

RESEARCH ARTICLE

Simulation and partial prototyping of an eight-junction holographic spectrum-splitting photovoltaic module

Sunita Darbe¹  | Matthew D. Escarra^{1,2}  | Emily C. Warmann¹  |
Harry A. Atwater¹ 

¹Thomas J. Watson Laboratories of Applied Physics, California Institute of Technology, Pasadena, CA, USA

²Department of Physics and Engineering Physics, Tulane University, New Orleans, LA, USA

Correspondence

Matthew D. Escarra, Department of Physics and Engineering Physics, Tulane University, New Orleans, LA, USA.

Email: escarra@tulane.edu

Funding information

National Science Foundation, Grant/Award Number: EEC-1041895; Office of Science, Grant/Award Number: DE-SC0001293; Advanced Research Projects Agency - Energy, Grant/Award Number: DE-AR0000333; Dow Chemical Company

Abstract

Spectrum-splitting photovoltaics incorporate optical elements to separate sunlight into frequency bands, which can be targeted at solar cells with bandgaps optimized for each sub-band. Here, we present the design of a holographic diffraction grating-based spectrum-splitting photovoltaic module integrating eight III-V compound semiconductor cells as four dual-junction tandems. Four stacks of simple sinusoidal volume phase holographic diffraction gratings each simultaneously split and concentrate sunlight onto cells with bandgaps spanning the solar spectrum. The high-efficiency cells get an additional performance boost from concentration incorporated using a single or a compound trough concentrator, providing up to 380X total concentration. Cell bandgap optimization incorporated an experimentally derived bandgap-dependent external radiative efficiency function. Simulations show 33.2% module conversion efficiency is achievable. One grating stack is experimentally fabricated and characterized.

KEYWORDS

holographic optical elements, III-V alloys, multijunction, photovoltaic, solar energy, spectrum splitting photovoltaics

1 | INTRODUCTION

Over 40% of solar power incident on a single-junction solar cell is lost due to two main causes. First, photons with energy less than the bandgap energy of the solar cell cannot be absorbed. Second, the excess energy of photons of higher energy than necessary to promote an electron from the valence band to the conduction band is lost as heat.¹ Two main strategies are used today to address these losses: conventional tandem multijunction photovoltaic systems and spectrum-splitting optical approaches. Both strategies attempt to prevent these losses by incorporating multiple absorbers of different bandgap energies in order to

absorb photons with reduced losses. Cutting-edge tandem multijunction solar cells hold the cell efficiency record of 47.1% power conversion efficiency for a six-junction cell under 143X concentrated AM1.5D illumination.² However, challenges include current-matching and lattice-matching constraints, and tunnel-junction design required for each additional bandgap added.³ Additionally, high concentration makes thermal management challenging. Finally, the series connection typical of multijunction solar cells causes an energy production penalty relative to independently connected subcells.⁴ Independent connection is easier to achieve through lateral spectrum splitting in which external optical elements are used to separate spectral bands.

This is an open access article under the terms of the Creative Commons Attribution License, which permits use, distribution and reproduction in any medium, provided the original work is properly cited.

© 2019 The Authors. *Energy Science & Engineering* published by the Society of Chemical Industry and John Wiley & Sons Ltd.

In addition to independent electrical connection, the thermal load of each cell is decreased thanks to their physical separation.

Many design concepts have been explored for spectrum-splitting photovoltaics including variations on a simple prism⁵ and mechanical stacking of solar cells such that wider bandgap cells act as absorption filters for narrower bandgap cells.⁶ Notably, Bragg reflectors are commonly used as spectrum-splitting optical elements. They can be designed to have sharp cutoffs in reflection or transmission to effectively separate spectral bands without overlap, similar to tandem multijunctions in which incident light to subsequent cells is filtered by the sharp absorption edges of higher bandgap cells.^{7,8} However, depositing many dielectric layers of precise thickness is time-consuming and costly. Holographic diffraction gratings, on the other hand, can be fabricated in a large area format at high fidelity. Dichromated gelatin (DCG), a common holographic recording medium, is highly transparent in the wavelength range of interest for photovoltaics⁹ and despite being hygroscopic can be quite durable under high-intensity illumination for extended periods when encapsulated.¹⁰

Efforts at two-way¹¹ and three-way splitting^{12,13} using holographic optics have been reported. Ingersoll and Leger¹¹ compare the results from stacked versus multiplexed sinusoidal gratings for two-way splitting. They address the dispersive behavior of holographic gratings by using multiple gratings either stacked or multiplexed to diffract different

portions of the same diffracted band. That is, they compare the performance of one grating diffracting a band from 500 to 900 nm to a range of diffraction angles from 11° to 22° to a pair of gratings in which one grating diffracts 480-620 nm to 14.5° to 18.5° and a second to diffract 700-900 nm light into the same angular range. Performance of stacked gratings is found to exceed the performance of two multiplexed gratings. Russo et al¹² report a 33.43% efficient optics and cell combination using GaAs, Si, and GaSb cells and an experimental holographic filter. The spectrum-splitting efficiency of this system is 87% given the reported 38.24% efficiency with ideal optics for the cell ensemble, where we define spectrum-splitting efficiency as

$$\eta_{SS} = \frac{\eta_{actual}}{\eta_{ideal}}, \quad (1)$$

where η_{actual} is the simulated or experimental system efficiency, and η_{ideal} is the efficiency of the system with perfect spectrum-splitting filters. To reduce dispersion losses, they use a “grating-on-lens” combination, which concentrates incident light to a spot size smaller than the the target solar cell. Thus, as the diffraction angle changes with wavelength throughout a given spectral band, most of the target frequency band still reaches the desired cell. Wu et al¹³ propose a variation on this concept using two cascaded simple sinusoidal gratings followed by a lens for three-way splitting. They project 46.9% power conversion efficiency for normally incident

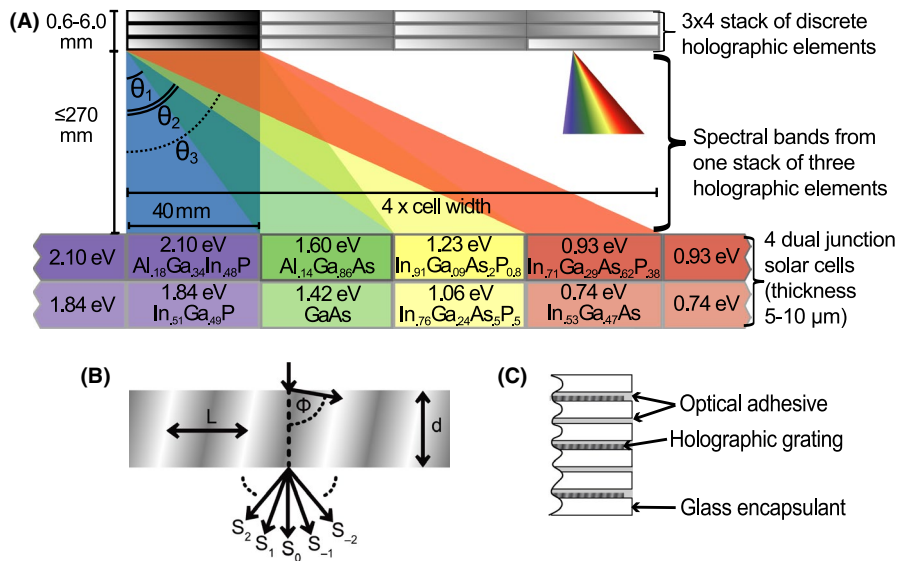


FIGURE 1 (A) Schematic of eight-junction holographic spectrum-splitting submodule, with cell bandgaps and III-V alloys indicated. Four stacks of three holographic gratings are assembled into a spectrum-splitting optical element. Each stack generates four spectral bands, one from each grating and the fourth composed of light that passes straight through the three-grating stack. Spectral bands are coupled into one of four high-efficiency III-V alloy, dual-junction solar cells tuned to best convert the target band of light (not to scale). The spectrum on the right shows dispersive nature of holographic splitting, (B) Schematic of volume phase hologram of thickness d with white and gray fringes representing varying refractive index with periodicity L , tilted with respect to the grating normal by angle Φ . Incident light is split into a series of diffracted orders S_i , and (C) Stack of three encapsulated holograms

light for experimental gratings with perfect cells and lossless concentration.

We opt to work with stacked sinusoidal volume Bragg gratings for simplicity over multiplexing, using a discrete set of 12 gratings in four parallel stacks. We aim to minimize optical interfaces, which can cause Fresnel reflections, and also to increase the number of subcells and the degree of concentration for highest efficiency. Thus, we incorporate eight subcells as four dual junctions and use a compound parabolic concentrator (CPC) for external concentration. We introduced this design concept, which uses a higher number of subcells than any previous effort, in prior work,^{14,15} where we also showed that larger numbers of subcells are necessary to achieve very high-efficiency photovoltaics. In this work, we present the detailed study of the potential for holographic spectrum splitting with stacked gratings and a larger number of subcells.

2 | DESIGN STRATEGY AND SIMULATION

The holographic spectrum splitter, shown schematically in Figure 1A, splits broadband, incident sunlight into four spectral bands, each targeted at a dual-junction solar cell with bandgaps tuned to best convert the spectral sub-band. The transmissive holographic spectrum-splitting optical element is composed of 12 asymmetric, individual volume phase holographic diffraction gratings arranged into four stacks of three gratings. Each grating in a stack is designed to primarily diffract one band of light, via its +1-diffracted order, toward one of the three solar cells not directly underneath the hologram stack. The fourth spectral band comprises light passing through the 0th diffracted orders of the three stacked gratings to the cell directly under the stack. Additionally, concentration is incorporated to boost module efficiency and to reduce cell area.

Our design strategy is to co-optimize multiple system elements for high module-level performance. This includes

optimization of the spectrum-splitting optics, the solar sub-cell bandgaps, and the concentrating optics. As an intermediate metric for evaluating spectrum-splitting performance, we use spectrum-splitting efficiency as defined in Equation (1).

2.1 | Grating simulation approach

The individual gratings have four design parameters, shown in Figure 1B: grating fringe tilt angle Φ , periodicity L , amplitude of index of refraction variation Δn , and grating thickness d . The splitting of the four λ_c of Stack 1, the grating stack on the left, is shown in Figure 1A. While shown as four discrete bands, the actual output is a continuous overlapping spectrum due to dispersive nature of holographic diffraction on broadband light as shown on the right. That is, the diffraction angle varies with wavelength, so wavelengths longer (shorter) than the design angle are diffracted to a higher (lower) angle than the target diffraction angle. Individual submodules are tiled one next to the other in both directions as shown in Figures 1A and 2A. The former shows the head-to-tail arrangement of successive four-tandem-cell submodules. The highest (lowest) energy bandgap of one submodule is adjacent to the highest (lowest) energy bandgap subcell of the next submodule. Due to the dispersive nature of the gratings, some light intended for each subcell ends up hitting the neighboring sub-cell instead. The head-to-tail arrangement allows light that is intended for the highest and lowest bandgap energy subcells but diffracted at too high of an angle to be collected in the neighboring submodule. Thus, this arrangement partially addresses the losses due to dispersive diffraction of holographic diffraction gratings.

Diffraction efficiency of individual holograms was simulated using generalized coupled-wave analysis¹⁶ implemented in MATLAB, since many of the gratings do not meet the Kogelnik criterion for being thick gratings.¹⁷ All simulations assume dichromated gelatin as the holographic medium. Calculations assume an average refractive index of 1.3 for dichromated gelatin (at the manufacturer's suggestion) and sinusoidal refractive index modulation. Fifteen diffracted

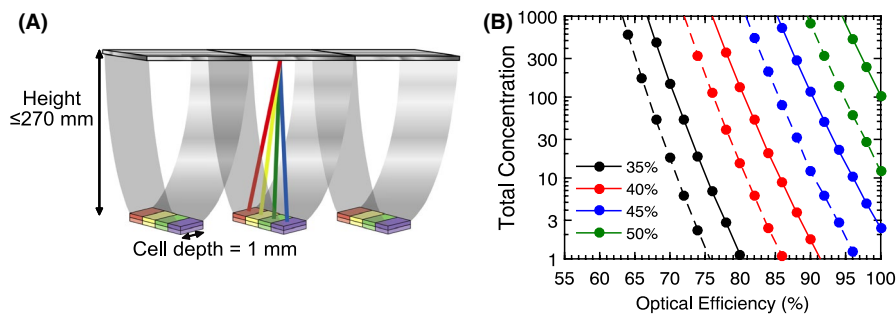


FIGURE 2 (A) Trough compound parabolic concentrators (CPCs) concentrate light in the direction orthogonal to spectrum splitting. Individual spectrum-splitting submodules tile to form a photovoltaic module and (B) Contours of 35%, 40%, 45%, and 50% module efficiency as a function of total concentration and optical efficiency for high (dashed) and moderate (solid) cell quality

orders were retained in the calculations, up to orders ± 7 . Stacked gratings were simulated by iterating the generalized coupled-wave model for subsequent gratings. The spectral and angular output of the first grating is the incident light into the second, and the output of the second grating is the input to the third grating. The incident solar illumination was assumed to be normal to the gratings. The simulated output of each hologram stack was converted to photon fluxes incident on each cell using a geometric calculation and weighting the output efficiency by the AM1.5D spectrum. Thus, the input to hologram simulations was the AM1.5D spectrum, while the input to cell calculations was the imperfect split output based on hologram simulations.

2.2 | Cell design

Optimized bandgaps and possible alloy compositions for an ideal split of the AM1.5D spectrum¹⁸ are indicated in Figure 1A. The subcells were selected by first identifying eight optimal single junction-bandgaps using a detailed balance model incorporating non-unity external radiative efficiency (ERE) and non-unity current collection efficiency as variable parameters to approximate realistic cell performance. The detailed method is described elsewhere.¹⁹ These eight bandgaps were combined into four pairs and adjusted to find lattice-matched dual junctions which are current matched in the case of perfect spectrum splitting. They are composed of group III-V semiconductor alloys. The two higher bandgap energy tandem cell alloys are latticed matched to GaAs as growth substrates, while the lower two are matched to InP. This ensemble of cells has a detailed balance efficiency of 63.0% at 25.3X concentration assuming perfect spectrum splitting and ideal material quality.

2.3 | Concentrator simulations

Using the eight ideal subcell bandgaps given in Figure 1A and the modified detailed balance model described above, iso-efficiency contours are calculated for 35%, 40%, 45%, and 50% module efficiency. The iso-efficiency lines are plotted in Figure 2B as a function of total concentration and optical efficiency (defined as the ratio of photons out to photons in for the system's optics) without considering the system geometry. The AM1.5D multiplied by the optical efficiency is simply used in the detailed balance model, so the losses are assumed to be spectrally independent. Total concentration includes both concentration incorporated through an external concentrator as well as through any concentration factor inherent to the spectrum splitting design. In the case of the current four-way splitting design, there is 4X internal concentration. Dashed lines show aggressive cell performance assumptions (3% ERE and 92.5% of ideal short circuit current J_{SC} collection efficiency) while solid lines have more moderate assumptions (1% ERE and 90% of ideal J_{SC}). The

plot gives the combined losses that can be tolerated for a given efficiency target. For highest efficiency, both high-optical performance of all components (including the splitting optics, the concentrator, the anti-reflection coatings, etc.) and high concentration are required.

Thus, concentration is incorporated orthogonal to the plane of spectrum splitting using a thermodynamically ideal trough CPC²⁰ which can double as a structural element holding the holograms in place above the cells. Employing a trough concentrator restricts the maximum degree of concentration to 100-200X for practical systems. The high angular spread of light in the splitting direction restricts our ability to incorporate a high degree of concentration along both axes. Concentrating elements were designed independently of the splitting optics using commercial ray tracing program LightTools.²¹

3 | OPTIMIZATION AND SIMULATION RESULTS

3.1 | Optical simulations

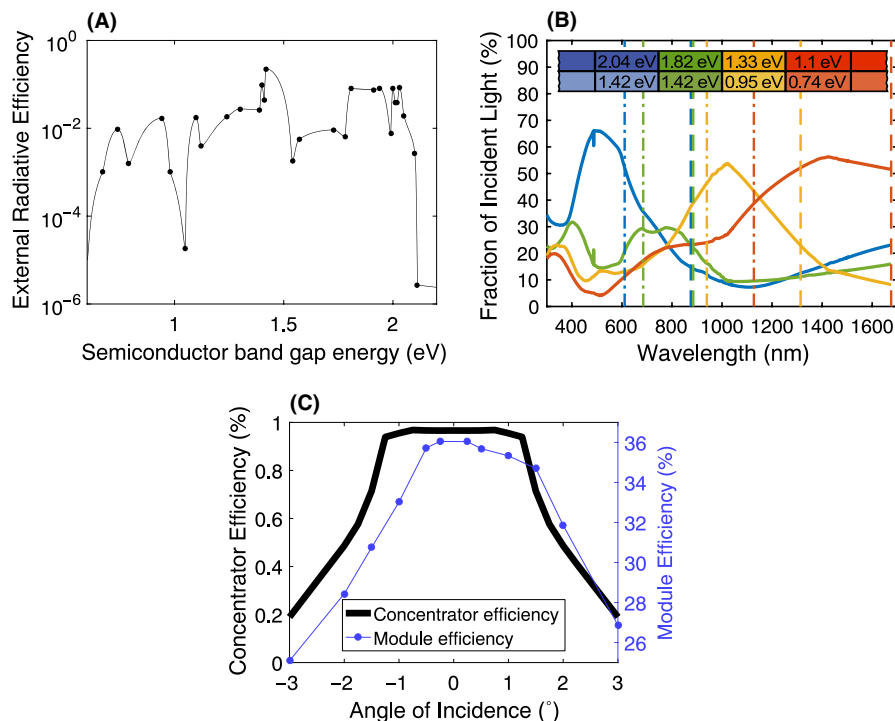
The optical simulations swept a range of parameters in search of an overall design capable of separating broadband sunlight into the desired sub-bands. In selecting the grating parameters, Φ and L are first chosen to fulfill the grating equation for the central wavelength λ_c of each spectral band for normally incident light. The $\lambda_{c,s}$ of the four ideal spectral bands are 487 nm, 774 nm, 1022 nm, and 1423 nm. The smallest diffraction angle within dichromated gelatin θ_1 is chosen to be 10° . While larger diffraction angles enable a smaller height-to-width ratio, they also increase the spread of angles hitting the solar cells, increasing the burden on the cell anti-reflection coatings to perform for a large angle range. Furthermore, diffraction angles larger than 50° within dichromated gelatin will lead to diffracted light being totally internally reflected if there is an air-encapsulant interface between the holograms and the cells. The other diffraction angles, determined by assuming constant cell width, are $\theta_2 = 19^\circ$ and $\theta_3 = 26^\circ$. The grating thicknesses were each selected to maximize the diffraction efficiency of λ_c going into the +1 diffraction order for a given Δn , subject to a maximum thickness constraint of $18 \mu\text{m}$ due to manufacturer limitations.

A parameter sweep was performed over Δn values and over the stacking order of the three gratings in each stack to optimize the value of a figure of merit which power weights the percentage of photons hitting the correct subcell. We define it as

$$\text{FOM}_i = V_i \times \text{flux}_i(\lambda) \times \eta(\lambda), \quad (2)$$

where $i = 1-4$ is the spectral band, V_i is an estimate for open-circuit voltage of subcell i calculated as the bandgap of the bottom subcell of the dual junction minus 400 meV, $\text{flux}_i(\lambda)$

FIGURE 3 (A) Experimentally derived, bandgap-dependent external radiative efficiency used for module design optimization, (B) Percentage of incident light hitting each of the four tandem solar cells after passing through the optimized holographic splitting element. Vertical lines correspond to the re-optimized bandgaps of the dual-junction solar cells that optimize device performance for the actual incident flux hitting each solar cell. Inset shows re-optimized bandgaps of four dual-junction cells based on actual spectral bands, and (C) Holographic splitter and concentrator performance as a function of incident angle. An incident angle range of $\pm 1^\circ$ is sufficient to retain $>93\%$ system performance, and performance drops off steeply by $\pm 2^\circ$



is the portion of the AM1.5D spectrum photon flux in band i , and $\eta(\lambda)$ is the fraction of in-band incident light reaching the solar cell. While the bandgap of the subcell minus 400 meV is a high-efficiency target for a single cell,³ we expect a higher voltage from the top cell of the dual junction, and the total voltage of the tandem is the sum of the voltages of the top and bottom subcells. Thus, V_i is slightly less than half the total voltage expected from cell i .

This figure of merit was evaluated for 58 wavelength points over the solar spectrum (300-1700 nm) with 24 nm spacing. Δn was varied between 0.01 and 0.06 by 0.005 increments for stacks 1 and 2 and between 0.015 and 0.055 by 0.01 increments for stacks 3 and 4 yielding up to 11 possible Δn values. Additionally, the three gratings could be stacked in six possible permutations. Each parameter combination was evaluated, and the results were sorted by FOM_i . The output fluxes of the eight best parameter combinations for each stack were combined and evaluated using a detailed balance re-optimization of the bandgaps for the actual flux hitting each cell (described below). The 20 best parameter sets for the holographic splitting element were then simulated with wavelength spacing of 1 nm.

3.2 | Bandgap re-optimization

Using the ideal bandgaps and holographic split spectrum, the resulting spectrum-splitting efficiency is 44%. Thus, to select among these 20 parameter sets, cell bandgaps were re-optimized using the modified detailed balance model to maximize system efficiency for the photon flux reaching

the cell plane after incident AM1.5D light was split by the holographic optical element. By the re-optimization process described in this section, spectrum-splitting efficiency was increased from 44% to 78%.

Non-unity ERE and non-ideal current collection as a percentage of J_{SC} were used to modify the Shockley-Queisser detailed balance model²² to get more realistic efficiency results. Published experimental cell voltages^{3,23,24} and experimental data from our lab²⁵ were used to develop a bandgap-dependent ERE for demonstrated III-V semiconductor alloys, shown in Figure 3A. We extracted ERE using the reciprocity relation,²⁶

$$V_{OC} = V_{OC, rad} + kT \ln ERE, \quad (3)$$

where V_{OC} is the experimental open-circuit voltage, $V_{OC, rad}$ is the open-circuit voltage expected in the radiative limit (internal radiative efficiency = 1) according to the Shockley-Queisser limit, k is the Boltzmann constant, and T is cell temperature. The data points used are included in a supplementary file. MATLAB's "pchip" interpolation function was used to create the curve shown in Figure 3A. The current collection efficiency is assumed to be 92.5% of above-bandgap incident flux due to contact shadowing, parasitic absorption, and imperfect current collection.

To re-optimize the subcell bandgaps for the simulated input fluxes, the top cell bandgap energy of each tandem cell was varied across all values for which reasonable III-V alloys latticed matched to InP or GaAs are available (0.72-2.1 eV). For each top cell value, a constraint to generate equal currents in the top and bottom junctions was used to find a

corresponding bottom bandgap. We allowed thinning of the top cell if a current-matched option could not be found without it. A lattice-matching constraint that restricted both top and bottom bandgap energies to either be above 1.42 eV for lattice matching to GaAs or both below 1.34 eV for lattice matching to InP was also implemented. Using the illumination spectrum on each cell originating from the holographic spectrum splitter, the tandem pair generating the highest power of all was selected.

3.3 | Results

Through the screening and bandgap re-optimization processes described above, an optimized set of grating specifications, given in Table 1, was determined. It is noteworthy that in three of four grating stacks one of the gratings ended up having the maximum thickness d (18 μm) and minimum Δn (0.01 for stack 1 and 0.015 for stacks 3 and 4). In grating stack 2, one grating has the maximum thickness and Δn just one step above the minimum (0.015). In some cases, especially for longer design wavelengths, these are quite weakly diffracting gratings. We decided to prototype the three gratings of Stack 1. The $\lambda_c = 1423$ nm grating of Stack 1 has the lowest effective thickness of all the gratings in the holographic splitting system. Thus, we fabricated and tested this stack with and without the $\lambda_c = 1423$ nm grating to determine its contribution to the spectrum splitting. The spectral separation of the four-stack holographic optical element is shown in Figure 3B, where the fraction of incident light hitting each of the four subcells is shown. The dashed vertical lines show the position of the absorption cutoffs for the top and bottom subcells re-optimized for the flux they are receiving under the holographic splitting element. The re-optimized bandgap energies are also given in the figure inset.

TABLE 1 Optimized holographic splitting element grating parameters

Stack no.	λ_c (nm)	Φ ($^\circ$)	L (μm)	d (μm)	Δn
1	1423	-77	2.43	18	0.01
	1022	-80.6	2.4	17.1	0.03
	774	-85	3.42	18	0.015
2	487	85	2.15	16.1	0.015
	1022	-85	4.51	18	0.015
	1423	-80.6	3.34	18	0.03
3	487	80.6	1.14	4.4	0.055
	1423	-85	6.28	18	0.045
	774	85	3.42	18	0.015
4	487	77	0.83	4.5	0.055
	1022	85	4.51	18	0.015
	774	80.6	1.82	18	0.015

The spectrum-splitting efficiency of this grating stack with re-optimized cells is 78%. The significant improvement from the initial value of 44% demonstrates the value of the optoelectronic co-optimization strategy.

Next, we studied the angular sensitivity of the system. We used the same simulation approach described in Section 2.1. However, instead of using normally incident light as the input to the first grating of each stack, we varied the input angle from -3° to 3° from normal in the splitting plane. The specular and angular output of the four grating stacks was converted to photon fluxes at the cell plane. Using these fluxes and the detailed balance cell simulation, we calculated the module efficiency as a function of incident angle without including concentrator or electrical losses and plotted the result in Figure 3C.

3.4 | Concentrator design

The module efficiency drops significantly outside of a roughly $\pm 2^\circ$ incident angle range due to holographic splitter performance as shown in Figure 3C. Thus, the concentrator was designed for a similarly tight acceptance half-angle. While trough CPC concentration only requires one-axis tracking, the holograms themselves are sensitive to angular variations in both directions. Thus, the system requires two-axis tracking. The angular spread of light exiting the concentrator is limited to 50° using a conical section at the CPC output to minimize Fresnel losses at the cell/concentrator interface.

Optimization was done by varying the CPC acceptance angle, the degree of truncation, and input aperture size. The output aperture size was fixed at 1 mm wide. The overall trough width depends on the CPC-height-to-cell-width ratio, which is constrained by the hologram diffraction angle and the refractive index of the CPC material given the other fixed geometrical parameters of the design. A hollow silver-coated trough, solid quartz trough, and solid PMMA trough CPC were each optimized. Finally, a two-stage CPC concentrator was simulated. The dual-stage concentrator comprised a primary silver-coated hollow trough which had its output coincident with the inputs of four rectangular solid CPCs that concentrated in both directions. The secondary concentrators were assumed to be made of lossless, high refractive index polymer with $n = 1.6$.^{27,28} The spectrum splitting itself incorporates an additional factor of up to 4X concentration in the case of ideal splitting since each spectral band is collected over an area of four holographic gratings and is output to a cell aperture that is as wide as one holographic grating in the spectrum-splitting direction. This component of concentration is accounted for in the hologram simulations.

The structure and transmission efficiency of the optimized concentrators are given in Table 2. The degree of concentration for the solid quartz trough is constrained by the

TABLE 2 Simulated concentrator parameters and optical transmission efficiency

Concentrator configuration	Suns	Trim	Height (mm)	Acceptance angle	Efficiency (%)
No external concentration	4X	n/a	n/a	n/a	100
Hollow trough CPC	101X	84%	173	1.1°	96.0
Solid quartz trough CPC	121X	77%	270	1.6°	97.4
Solid PMMA trough CPC	19X	94%	7	5°	95.4
Hollow trough CPC with solid, 2-axis secondary CPC (hollow/solid)	380X	81%/0%	186/6	1.5°/19°	91.7

height of the concentrator. We chose to limit the height of the concentrator to about 270 mm for a total module height of about 300 mm as a practical constraint. For the solid PMMA trough, the concentrator height is limited by optical losses due to absorption in the polymer. The height in this case is 7 mm giving a power-weighted solar absorption of 3.3% in the concentrator material. On the other hand, the hollow silver-coated trough CPC incurs metal absorption losses rather than volumetric losses, so the height can be extended to 173 mm. However, higher transmission efficiencies are achieved with a higher degree of truncation as less light hits the silver surface at grazing incidence, minimizing absorption to 2.7%. The concentrator efficiency plotted in Figure 3C is the transmission efficiency of the hollow silvered trough CPC as the half-angle of the incident light cone is increased from 0° to 3°. The acceptance angles of the modeled concentrators are $\geq 1.1^\circ$. As with the angle sensitivity of the gratings in the splitting direction, this falls within the error tolerance of standard closed-loop sun trackers. The concentrator efficiency is crucial to system efficiency as concentrator losses directly reduce cell current and thereby also cell voltage. Thus, increasing the degree of concentration at the expense of the concentrator transmission efficiency does not pay off for system efficiency.

4 | EXPERIMENTAL APPROACH AND RESULTS

4.1 | Approach

The three gratings of Stack 1 (the hologram stack above the highest bandgap energy tandem cell) were fabricated ($n = 4$ each). The diffraction efficiency of each grating and the grating stack was measured as a function of diffraction angle and wavelength for normally incident light using the Scatterometry feature of a J. A. Woollam Variable Angle Spectroscopic Ellipsometer (V-VASE), which outputs monochromatic light with divergence of $< 0.3^\circ$. Holograms were fabricated by Wasatch Photonics as a best effort to match our specifications. The holographic recording medium, dichromated gelatin, is hygroscopic and must be encapsulated

for the holographic diffraction grating to persist. Thus, the individual gratings are encapsulated and combined into a stack using optical adhesive (Figure 1C). The holographic recording medium is deposited on a 1 mm fused silica slide (thickness chosen for ease of handling). A second slide is coated with Norland Optical Adhesive (NOA) to adhere it to the dichromated gelatin and glass substrate as an encapsulating superstrate. In order to estimate internal transmission and diffraction efficiency, the total collected light data from hologram measurements were treated to remove Fresnel reflections from the front and back air/fused silica interfaces without anti-reflection coatings, according to

$$T_c = \frac{T_m(\lambda, \theta)}{(1 - R_f) \times (1 - R_b(\lambda, \theta))}, \quad (4)$$

where T_c is the corrected total transmission assuming perfect front and back anti-reflection coatings; T_m is the total measured transmission; $R_f(\lambda)$ is the front air/fused silica Fresnel reflection which depends only on wavelength λ since the light is normally incident; and $R_b(\lambda, \theta)$ is the back surface, angle and wavelength-dependent reflection.

4.2 | Results

4.2.1 | Individual grating and grating stack performance

The diffraction efficiency at normal-incidence illumination of the four fabricated $\lambda_c = 1022$ nm gratings (one of the three Stack 1 gratings detailed in Table 1) is shown in Figure 4. The first-order diffraction peak falls close to 1022 nm, as designed. At the peak, 100% of transmitted light is going into the first diffracted order, demonstrating the high diffraction efficiency potential of volume holographic gratings. The presence of diffracted orders +2, +3, and +4 validates the choice of generalized coupled-wave analysis rather than a simpler simulation framework for the holograms. The red shift of about 40 nm of the first-order diffraction peak of gratings A, B, and D in comparison with grating C could be due to swelling in the DCG during development.

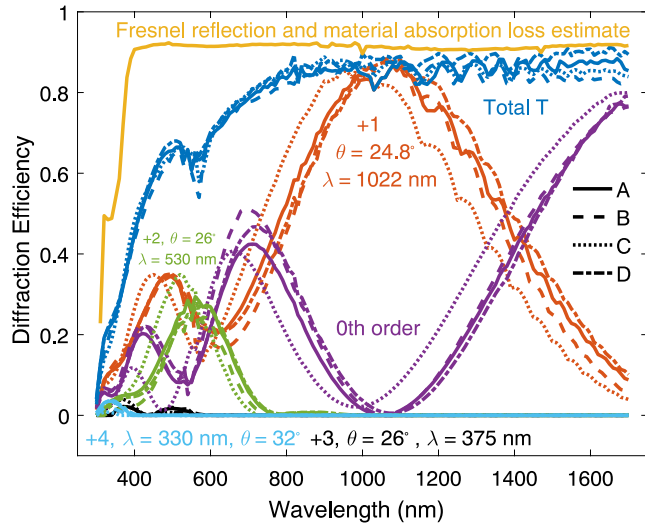


FIGURE 4 Measurement results for four $\lambda_c = 1022$ nm gratings. Each line style represents a different grating and each color shows a different diffracted order. The order, peak wavelength and diffraction angle for each order are noted as well as an approximation of Fresnel reflection and DCG and NOA material absorption losses in yellow at the top

In addition to diffraction efficiency of individual orders, the summed transmission *Total T* is shown. There is a large deviation between the total collected light and the anticipated light collection, represented in Figure 4 by the yellow loss estimate line which accounts for back-reflected light at the fused silica/dichromated gelatin and fused silica/air interfaces as well as material absorption in the DCG and NOA layers. These additional losses are due to a combination of scattering within the dichromated gelatin, multiple diffractions leading to light being trapped within the grating layer, and optical artifacts from the recording process.

The total transmitted light through the $\lambda_c = 774$ nm and $\lambda_c = 1423$ nm gratings was measured in the same way. Uncollected light is due to lack of anti-reflection coatings at the air-glass interfaces at the front and back interfaces of the holograms and to scattering and absorption within the hologram. In order to isolate the scattering and absorption losses, the Fresnel transmission losses were calculated and divided out of the *Total T*. The Fresnel-corrected transmission spectra of all the measured gratings are averaged to estimate an experimental transmission correction, which serves as a proxy for all unaccounted for experimental losses. Figure 5A shows this experimental correction factor. By squaring and cubing the experimental correction factor, we get the “two-grating correction” and “three-grating corrections”, respectively.

The best grating of each λ_c was included in the full stack. The 774 nm grating and 1022 nm grating were first glued together into a two-grating stack and characterized, and then, the 1423 nm grating was added and the three-grating stack measured. The *Total T* of the stacks was measured and is also

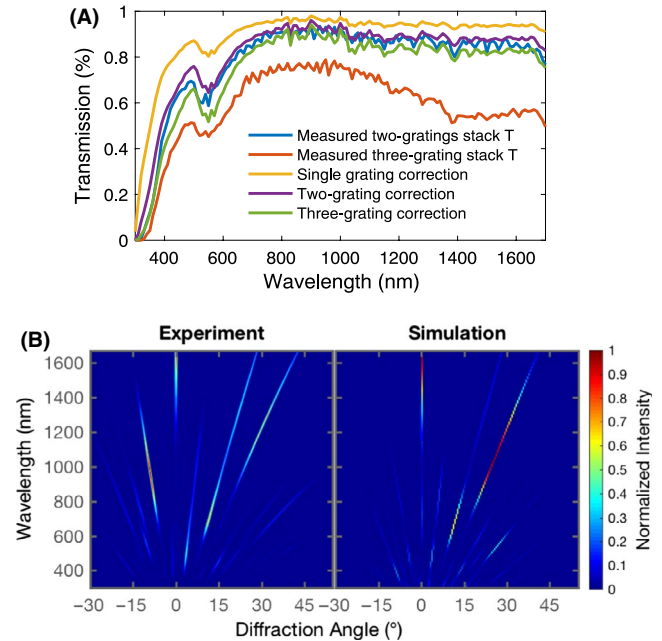


FIGURE 5 (A) Average transmission through 11 of the 12 experimentally fabricated gratings after Fresnel correction is applied. Also plotted is this same transmission squared and cubed to approximate transmission through two and three-grating stacks. Also shown are the measured, Fresnel corrected transmission for the two and three-grating stacks and (B) Color plots showing spectral and angular spread of (left) measured and (right) simulated light going through grating Stack 1

plotted in Figure 5A. The dip around 550 nm, observed in all the gratings, is not a material absorption of either the optical adhesive or dichromated gelatin. Possible sources of this dip include optical recording artifacts and absorption of chromium that has not been properly cleaned out of the recording plate during development. The experimental two-grating stack curve and the calculated two-grating correction show quite similar total transmission, suggesting that the transmission losses of the two grating stack are well accounted for by losses observed in the individual gratings. On the other hand, the experimentally measured three-grating stack transmission is lower than the three-grating correction. Some other loss mechanisms, potentially misalignment of the grating stacks, are at work.

Figure 5B shows color plots of normalized diffraction efficiency versus wavelength and diffraction angle for the experimental and simulated grating stacks. In both plots, light is diffracted to angles between 10° and 40° across the solar spectrum. However, the most notable difference is a diffracted order peaking around 900 nm and -15° . Measurements indicate that this is due to the 774 nm grating re-diffracting some of the 1st diffracted order of the 1022 nm grating. Since the grating simulation code used the diffracted orders of the first grating as the input to the second grating, cross-talk was accounted for in the simulations. Thus, this unintended

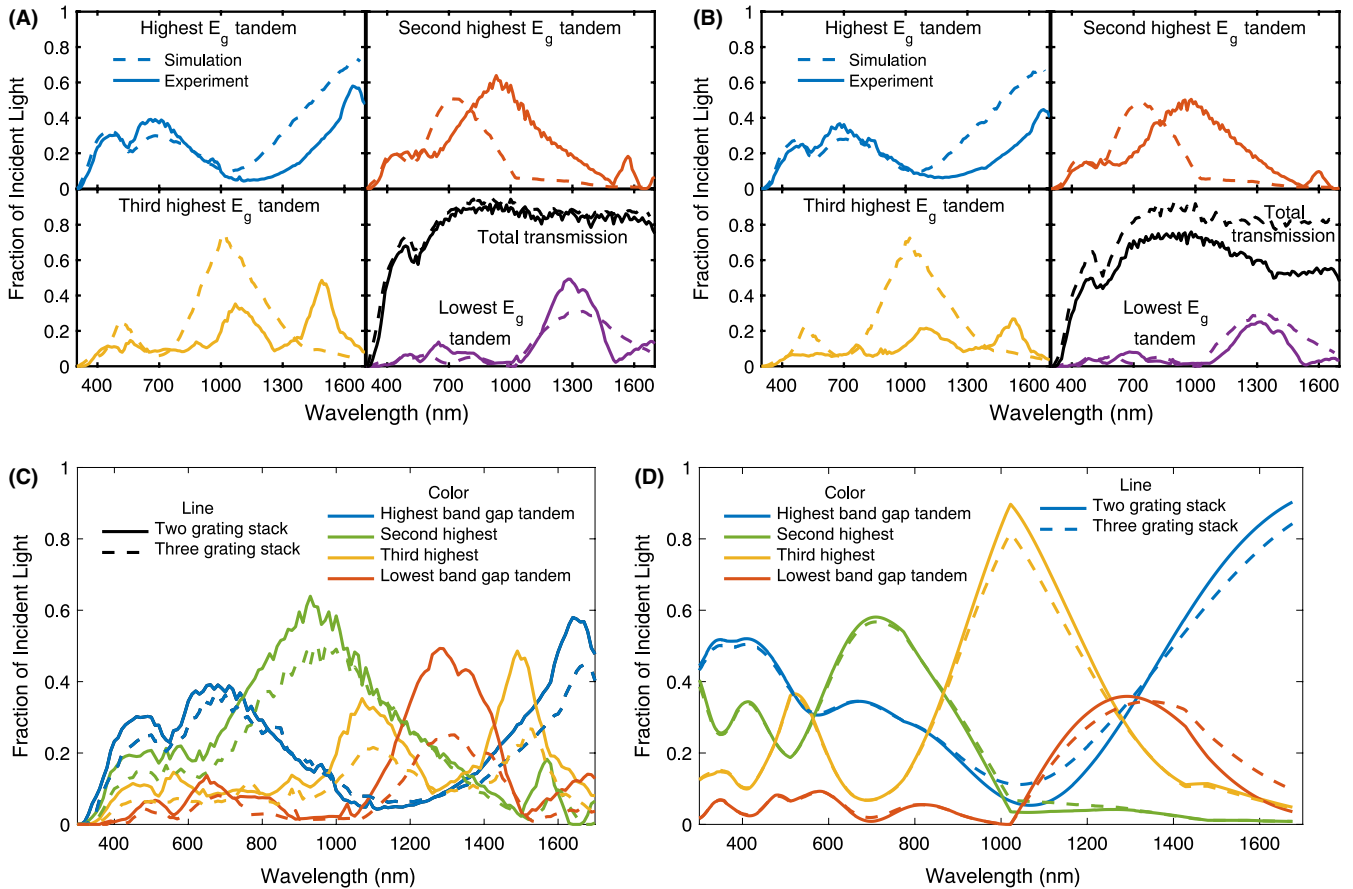


FIGURE 6 (A, B) Experimentally measured diffraction efficiency of (A) two and (B) three-grating hologram stack converted to fraction of incident light as a function of wavelength that would be incident on each tandem cell plotted with equivalent simulation results (dashed). The bottom right panel also shows the total transmitted light collected that would go into any of the tandem cells and (C) Experimentally measured and (D) simulated fraction of light going into each subcell versus wavelength for two-grating versus three-grating stack. While the simulated differences are minimal, there is greater transmission loss for the experimental, three-grating stack

cross-talk suggests a discrepancy between the simulated and experimentally fabricated grating. This is perhaps due to a deviation from perfectly sinusoidal grating fringes.

During the fabrication process, individual gratings were illuminated at normal incidence, and their primary peak's wavelength and position were used as a quality check. In the future, the interaction of the main diffracted orders with subsequent gratings should also be verified during grating recording and development to avoid this issue. These experimental gratings represent a first attempt to experimentally verify our design assumptions, and further refinement is necessary by iterative optimization of grating design and fabrication. Thus, these experimental data provide a lower bound for potential performance, which can inform future design work.

4.2.2 | Two-grating versus three-grating stack comparison

The fraction of photons incident on the holographic splitting element that are diffracted onto each subcell, determined by

simulation and experiment for the initial two-grating stack are shown in Figure 6A. As above, this dataset was converted from intensity leaving the hologram plane to flux hitting the subcells by propagating the diffracted light to the cell plane and weighting by the AM1.5D reference spectrum. The three-grating stack results are shown in Figure 6B. In both cases, the total transmitted light is shown in the bottom right panel. The experimentally measured results (solid lines) were corrected to remove front and back surface Fresnel reflections according to Equation (4). The simulated results (dashed lines) are adjusted by multiplying the two-grating and three-grating corrections.

The main source of loss, after accounting for absorption, scattering, and Fresnel reflection losses, is the cross-talk discussed above, causing the diffracted order at 900 nm/ -15° . Because of this unintended diffracted order, much of the light intended for the third highest bandgap energy tandem cell ends up in the second highest instead, as can be seen in Figure 6A.

Figure 6C shows the fraction of light that would enter each of the four tandem solar cells passing through the

	PCE (%)
Ideal cells, ideal optics Unity ERE and 100% J_{SC}	63.0
Derated cells, ideal optics Modified detailed balance cells with non-unity ERE and 92.5% J_{SC} , ideal spectrum splitting	52.3
Derated cells, simulated splitting Original modified detailed balance cells, simulated HOE splitting, no additional losses	23.0
Re-optimized derated cells, simulated splitting Cells re-optimized for the simulated HOE splitting	40.8
+Internal losses (12% relative) – Fresnel reflection loss and NOA and DCG material absorption losses	36.0
Projected module efficiency + external losses: 25.3X hollow trough concentrator and electrical combination losses	33.2

TABLE 3 Holographic spectrum splitter module power conversion efficiency (PCE)

experimentally made two- and three-grating stacks. Across all wavelengths for each of the cells, less light is collected in the three-grating case due to increased scattering, the higher number of interfaces, and possibly due to misalignment as mentioned above. Given the unaccounted for experimental losses and the small performance benefit from the 1423 nm grating even in the simulated results (shown in Figure 6D), the two-grating stack better separates solar illumination into four spectral bands. The small difference between the two- and three-grating cases is due to the diffraction angle versus wavelength of the 1022 nm and 1423 nm gratings being the same with the diffraction efficiency of the 1022 nm grating being much higher. The bandwidth of the 1022 nm grating is high enough to diffract the lowest frequency band also. The measured FWHM of the 1st order diffraction peak is 600 nm while the target diffraction band is 300 nm wide. As the wavelength of the light passing through this grating increases from λ_c , the diffraction angle also increases, sending this light into the lowest bandgap tandem and alleviating the need for a separate grating to perform this function.

In the experimental holograms, many transmission losses are not inherent to dichromated gelatin or the grating design. This is especially true of the dip around 550 nm and the unintended diffracted order causing spectral mismatch from simulation. They would be addressed in remaking the gratings. Because of this, using these experimental results to project module efficiency only gives a lower bound rather than a realistic estimate. For example, if we apply the two-grating correction to the simulated photon flux and calculate the module efficiency as presented in Table 3 below including all internal and external losses, the final efficiency would be 28.7%. A key lesson from this first experimental demonstration shows that aiming for a large number of subcells does not require as high a number of holographic gratings. Future iterations, rather than having a grating for each spectral band, should aim to use as few gratings as possible to split the spectrum in order to avoid interface and interaction losses.

5 | MODULE EFFICIENCY PROJECTION

Finally, we project a module power conversion efficiency (PCE) for this eight-junction holographic splitting, concentrating photovoltaic module design. Holographic splitting element and concentrator ray-tracing simulation results were combined with estimates of anticipated losses. The simulations account for misallocation of light due to the holographic splitting. Next, material absorption and Fresnel losses were incorporated. Absorption of DCG was extracted from published internal transmittance data.⁹ NOA 88, used to glue the gratings into a stack as well as attaching the superstrate of each grating, is assumed to be index matched. NOA absorption was measured and incorporated in efficiency projections. We assume optimistically high-performance anti-reflection coatings giving a total of 5% Fresnel losses combined for the front air/hologram interface, the hologram/CPC interface, and the CPC/cell interfaces. For the front air-fused silica interface, the normal-incidence transmission of an optimized anti-reflection coating is assumed to be 99% across the solar spectrum. At the back air-fused silica interface with an additional need for anti-reflection for a broad angle range, a transmission of 98.5% is assumed.²⁹ Finally at the cell input face, an angle and spectral averaged transmission of 97.5% is assumed for a total of 5% Fresnel reflection losses. Finally, simulated concentrator transmission efficiency and electrical efficiency are included. DC-DC power conditioning efficiency of 98%³⁰ and 2% series resistance loss is included. DC-DC power conditioning is used to combine the power from the four independently electrically connected subcells. With independent connection, we can take advantage of the whole spectrum even as it changes throughout the day.⁴

Results of this projection are shown in Table 3. While the detailed balance efficiency of the cell ensemble for perfect splitting is 63.0%, many losses are incurred in the

multicomponent system. Accounting for realistic cell materials using the modified detailed balance model brings the efficiency potential down to 52.3% with perfect spectrum splitting. Using the same ideal cells for the achieved spectrum splitting drops the efficiency to 23.0%, while re-optimizing the cells for the spectrum-splitting performance gives 40.8% efficiency. This demonstrates the value of co-optimizing cells and optics in a spectrum-splitting system. Next, “internal” system losses are included—Fresnel reflection losses and material absorptions of NOA and DCG. Incorporating “external” factors—concentrator and electrical efficiency, we project a module efficiency of 33.2% for the 25.3X hollow silver-coated trough. Using Improvement over Best Bandgap, a metric defined by Russo et al¹² to compare different spectrum-splitting systems, we find that our calculated eight-junction spectrum splitter internal efficiency of 36.0% of Table 3 represents a relative improvement of 25% compared to the 28.8% record single-junction GaAs cell of Alta Devices ($36.0/28.8 = 1.25$) and a relative improvement of 18% compared to the 30.5% record GaAs (258x) concentrator cell of NREL ($36.0/30.5 = 1.18$).³¹

6 | OUTLOOK

Improving spectrum-splitting efficiency, especially through more accurately separating the spectral bands, is the most direct path to higher module efficiency. Thicker, lower Δn gratings could give narrower bandwidths, but lower Δn (<0.005) gratings are not accessible in dichromated gelatin. Additionally, lower Δn requires higher thickness to maintain the necessary effective thickness to achieve high diffraction efficiency. However, high thickness leads to increased scattering. For comparable effective thickness, lower Δn would give a narrower bandwidth, minimizing cross-talk between different spectral bands and suppressing diffraction into unintended diffraction orders. There are photopolymers and glass-based photo-reactive³² materials, which allow Δn a couple of orders of magnitude lower than DCG, with thickness on the order of millimeters, which could give few nm wide diffraction bandwidths, but media with just a slightly lower Δn are not readily available.

Regardless of the material, individual volume phase holographic grating diffraction profiles can have quite high peak diffraction efficiency at the intended angle and λ_c . This is evident in Figure 4. At its peak, >99% of light transmitted through the 1022 nm λ_c grating is going into the first diffracted order. As the incident angle or wavelength varies from the intended angle of incidence and from λ_c , however, diffraction efficiency decreases. Additionally, the diffracted orders aside from the 0th order are dispersive. As such, the angle at which light is diffracted varies with wavelength. Both of these factors lead to the sloped fraction of light profiles in

Figure 3B, and thus the overlap of top and bottom bandgaps of adjacent tandem subcells' bandgaps after re-optimization for actual splitting.

Ultimately, the sloped rather than square diffraction profile and dispersion of the diffracted orders are an impediment to high spectrum-splitting efficiency using holograms. The strategy of Russo et al¹² to incorporate concentration after splitting to overcome dispersion seems compatible with our splitting design for future iterations to increase efficiency.

The main challenge to adoption of spectrum-splitting and other non-single junction technologies is manufacturing complexity. As such, this design has significant drawbacks for commercial deployment. The larger number of components each leads to small losses that can chip away at the final module efficiency. The fact that our two-grating stack performance exceeded that of the three-grating stack due to alignment and additional transmission losses underscores the need to factor complexity and the costs of complexity into the design process. Based on this work, an updated design with two gratings per stack and three dual-junction cells are worth further exploration. Additionally, CPCs were explored for concentration in order to decrease the number of optical interfaces (eg quartz CPC) and decrease absorption relative to molded plastic lens concentrators. Indeed, the solid quartz CPC has the highest concentrator efficiency. However, fabrication of perfect glass surfaces and especially the accurate shape necessary at the cell output face, especially at the proposed size scale is quite difficult. Concessions such as moving from thermodynamically ideal CPCs to more manufacturable lenses are required. Optoelectronic design and assembly technologies employed in displays, for example, could be employed to decrease complexity in the assembly process. For example, automated pick and place machinery can be used to assemble and electrically connect the many components.

Recently, cost gains in photovoltaics have benefited from non-technical achievements such as supply chain improvements in the solar industry. One-axis tracking has become more wide spread, leading to cost advantages from scale. Once these types of improvements are exhausted, efficiency improving technologies will again become more important for pushing \$/W costs lower. Further work on holographic spectrum splitting should focus on incorporating high-quality cells with a dispersion reducing strategy such as concentrating to an area smaller than the cell.

7 | CONCLUSION

We present the design of a holographic diffraction grating-based spectrum-splitting concentrating photovoltaic module incorporating four dual-junction tandem III-V solar cells with simulated module efficiency of 33.2%. This design is the first

holographic diffraction system to incorporate eight solar sub-cells. While cell efficiency potential is quite high, dispersion in the splitting optics limits module efficiency. Additionally, while experimental demonstration of one of four three-grating stacks shows a good match with simulated targets for individual gratings, a spurious diffracted order appears when the gratings are stacked. Addressing the dispersion issue is the main barrier to high module efficiency for holographic spectrum splitting systems.

ACKNOWLEDGMENTS

The optical design was supported by the US Department of Energy (DOE) "Light-Material Interactions in Energy Conversion" Energy Frontier Research Center under grant DE-SC0001293; the experimental work was supported by Advanced Research Projects Agency–Energy, DOE, under Award Number DE-AR0000333; the work of ECW was supported by the National Science Foundation (NSF) and DOE under NSF CA No. EEC-1041895. Any opinions, findings and conclusions or recommendations expressed in this material are those of the authors and do not necessarily reflect those of NSF or DOE. The work of MDE and SD was supported by Dow Chemical Company.

The authors would like to thank D. Speer at Wasatch Photonics for hologram fabrication and R. Synowicki at J. A. Woollam, W. Zhou and R. Feist of Dow Chemical Company, and C. A. Flowers and N. Batara for useful discussions.

ORCID

Sunita Darbe  <https://orcid.org/0000-0002-8099-1814>

Matthew D. Escarra  <https://orcid.org/0000-0002-0232-942X>

Emily C. Warmann  <https://orcid.org/0000-0002-2810-4608>

Harry A. Atwater  <https://orcid.org/0000-0001-9435-0201>

REFERENCES

- Polman A, Atwater HA. Photonic design principles for ultrahigh-efficiency photovoltaics. *Nat Mater*. 2012;11(3):174-177.
- National Renewable Energy Laboratory. Best research-cell efficiency chart. <https://www.nrel.gov/pv/cell-efficiency.html>. Accessed July 14, 2019.
- King RR, Bhusari D, Boca A, et al. Band gap-voltage offset and energy production in next-generation multijunction solar cells. *Prog Photovolt Res Appl*. 2011;19(7):797-812.
- Warmann EC, Atwater HA. Energy production advantage of independent subcell connection for multijunction photovoltaics. *Energy Sci Eng*. 2016;4(4):235-244.
- Li D, Michel J, Juejun HU, Tian GU. Compact spectrum splitter for laterally arrayed multi-junction concentrator photovoltaic modules. *Opt Lett*. 2019;44(13):3274-3277.
- Akira Ishibashi H, Kobayashi T, Taniguchi KK, Kasai T. Optical simulation for multi-stripped orthogonal photon-photocurrent-propagation solar cell (MOP3SC) with redirection waveguide. *3D Res*. 2016;7(4):33.
- Wang X, Waite N, Murcia P, et al. Lateral spectrum splitting concentrator photovoltaics: direct measurement of component and submodule efficiency. *Prog Photovolt Res Appl*. 2012;20(2):149-165.
- Eisler CN, Flowers CA, Warmann EC, et al. The polyhedral specular reflector: a spectrum-splitting multijunction design to achieve ultrahigh (>50%) solar module efficiencies. *IEEE J Photovolt*. 2019;9(1):174-182.
- Ebizuka N, Kawabata KS, Oka K, et al. Grisms developed for FOCAS. *Publ Astron Soc Japan*. 2011;63(sp2):S613-S622.
- Hariharan P. *Optical Holography: Principles, Techniques and Applications*, 2nd edn. New York City, NY: Cambridge University Press; 1996.
- Ingersoll GB, Leger JR. Optimization of multi-grating volume holographic spectrum splitters for photovoltaic applications. *Appl Opt*. 2016;55(20):5399-5407.
- Russo JM, Zhang D, Gordon M, Vorndran S, Yuechen WU, Kostuk RK. Spectrum splitting metrics and effect of filter characteristics on photovoltaic system performance. *Opt Express*. 2014;22(S2):A528-A541.
- Yuechen WU, Chrysler B, Kostuk RK. Design and fabrication of cascaded dichromate gelatin holographic filters for spectrum-splitting PV systems. *J Photon Energy*. 2018;8(1):017001.
- Escarra MD, Darbe S, Warmann EC, Atwater HA. Spectrum-splitting photovoltaics: holographic spectrum splitting in eight-junction, ultra-high efficiency module. IEEE Photovoltaic Specialists Conference (IEEE). 2013;1852-1855.
- Darbe S, Escarra MD, Warmann EC, Atwater HA. Holographic spectrum splitter for ultra-high efficiency photovoltaics. *Proc SPIE*. 2013;8821:882105.
- Magnusson R, Gaylord TK. Analysis of multiwave diffraction of thick gratings. *J Opt Soc Am*. 1977;67(9):1165-1170.
- Kogelnik H. Coupled wave theory for thick hologram gratings. *Bell Syst Tech J*. 1969;48(9):2909-2947.
- ASTM G173-03. *Standard Tables for Reference Solar Spectral Irradiances: Direct Normal and Hemispherical on 37° Tilted Surface*. West Conshohocken, PA: ASTM International; 2012. www.astm.org.
- Warmann EC, Flowers C, Lloyd J, Eisler CN, Escarra MD, Atwater HA. Design of photovoltaics for modules with 50% efficiency. *Energy Sci Eng*. 2017;5(2):69-80.
- Winston R. Light collection within the framework of geometrical optics. *J Opt Soc Am*. 1970;60(2):245-247.
- LightTools (Version 8.3) [Software]. Mountain View, CA: Synopsys Inc.; 2013.
- Shockley W, Queisser HJ. Detailed balance limit of efficiency of p-n junction solar cells. *J Appl Phys*. 1961;32(3):510-519.
- Perl EE, Simon J, Geisz JF, et al. Development of high-bandgap AlGaInP solar cells grown by organometallic vapor-phase epitaxy. *IEEE J Photovolt*. 2016;6(3):770-776.
- Geisz JF, Steiner MA, García I, Kurtz SR, Friedman DJ. Enhanced external radiative efficiency for 20.8% efficient single-junction GaInP solar cells. *Appl Phys Lett*. 2013;103:041118.

25. Lloyd J. Optoelectronic design and prototyping of spectrum-splitting photovoltaics. PhD dissertation. Chap 5, pg 97. California Institute of Technology; 2018 <http://resolver.caltech.edu/CaltechTHESIS:05212018-185007265>
26. Ross RT. Some thermodynamics of photochemical systems. *J Chem Phys.* 1967;46(12):4590-4593.
27. Liu J-G, Ueda M. High refractive index polymers: fundamental research and practical applications. *J Mater Chem.* 2009;19(47):8907-8919.
28. Macdonald EK, Shaver MP. Intrinsic high refractive index polymers. *Polym Int.* 2015;64(1):6-14.
29. Yao Y, Lee K-T, Sheng X, et al. Porous nanomaterials for ultra-broadband omnidirectional anti-reflection surfaces with applications in high concentration photovoltaics. *Adv Energy Mater.* 2017;7(7):1601992.
30. Agamy MS, Chi S, Elasser A, et al. A high-power-density DC-DC converter for distributed pv architectures. *IEEE J Photovolt.* 2013;2:791-798.
31. Green MA, Hishikawa Y, Dunlop ED, et al. Solar cell efficiency tables (version 53). *Prog Photovolt Res Appl.* 2019;27(1):3-12.
32. Efimov OM, Glebov LB, Glebova LN, Richardson KC, Smirnov VI. High-efficiency Bragg gratings in photothermorefractive glass. *Appl Opt.* 1999;38(4):619-627.

SUPPORTING INFORMATION

Additional supporting information may be found online in the Supporting Information section at the end of the article.

How to cite this article: Darbe S, Escarra MD, Warmann EC, Atwater HA. Simulation and partial prototyping of an eight-junction holographic spectrum-splitting photovoltaic module. *Energy Sci Eng.* 2019;00:1–13. <https://doi.org/10.1002/ese3.445>